PCCP

ROYAL SOCIETY OF CHEMISTRY

PAPER

View Article Online
View Journal | View Issue

Cite this: *Phys. Chem. Chem. Phys.*, 2025, **27**, 25127

Uncovering elusive ultrafast charge transfer-driven structural changes in 4,4′-bis(9-carbazol-9-yl)-1,1′-biphenyl, a paradigmatic molecular triad

Jungkweon Choi, †[ab] Donghwan Im, †[ab] Jeong Hoon Lee, [ab] Alekos Segalina [ab] and Hyotcherl Ihee *[ab]

Received 8th September 2025,
Accepted 6th November 2025

DOI: 10.1039/d5cp03464g

rsc.li/pccp

Organic semiconductors have attracted significant attention for their potential in flexible, lightweight, and tunable optoelectronic applications. Among them, 4,4′-bis(9-carbazol-9-yl)-1,1′-biphenyl (CBP) is one of the most widely employed host materials. However, despite its extensive applications, its intrinsic excited-state dynamics and subsequent structural evolution remain underexplored. In this study, we combined femtosecond transient absorption (fs-TA) spectroscopy and nonadiabatic molecular dynamics (NAMD) simulations to investigate the excited-state dynamics of CBP. A comprehensive analysis of fs-TA data obtained in solvents with varying polarity and viscosity, combined with NAMD simulations, reveals a sequential progression of excited-state structural rearrangements. Specifically, we find that intramolecular charge transfer from the carbazole to the biphenyl unit occurs on a sub-picosecond timescale, followed sequentially by biphenyl planarization accompanied by a slower torsional motion around the bond connecting the biphenyl and carbazole moieties. Notably, the vibrational energy redistribution between torsional vibrational modes is identified as a key factor governing the stepwise structural evolution. These findings provide new insight into the excited-state dynamics of CBP and offer design guidelines for the development of next-generation OLED host materials.

Introduction

Organic electronic devices, such as organic light-emitting diodes (OLEDs), organic photovoltaics (OPVs), and organic field-effect transistors (OFETs), have emerged as key technologies in modern optoelectronics.[1–11] Their tunable properties, mechanical flexibility, and ability to operate without relying on scarce and expensive metals make them particularly attractive. Achieving high performance in these systems requires a comprehensive understanding of the fundamental processes governing charge transport within the devices, as they are closely linked to the excited-state dynamics of the active materials. These processes unfold on ultrafast timescales, ranging from femtoseconds to picoseconds, including structural relaxation, radiative decay, and excimer formation.[12–20] A detailed understanding of these excited-state processes is therefore essential, as they directly impact charge generation, recombination and transport. Therefore, clarifying the interplay between excited-state processes and molecular structural evolution is essential to fully elucidate the mechanisms underlying charge transport in these systems.[21–23]

In this context, 4,4′-bis(9-carbazol-9-yl)-1,1′-biphenyl (CBP) has attracted considerable attention due to its well-balanced hole/electron transport properties, high thermal stability, and excellent compatibility with a wide range of guest emitters.[24–31] Its donor–acceptor–donor (D–A–D) architecture, comprising two electron-donating carbazole units symmetrically linked to a central electron-accepting biphenyl core, facilitates efficient intramolecular charge transfer (ICT), enhancing charge mobility. Owing to these favorable characteristics, CBP has been established as a benchmark host material in phosphorescent OLEDs (PhOLEDs) and related optoelectronic applications based on host–guest architectures, thus motivating extensive investigations into its photophysical and charge transport properties.

To better understand the relationship between molecular structure, photophysical behavior, and charge transport in organic electronic devices, several studies have employed molecular engineering strategies, such as introducing functional groups to restrict conformational flexibility. Previous studies, including those by Köhler *et al.*, have shown that CBP undergoes excited-state planarization, leading to red-shifted emission relative to more conformationally restricted analogues such as

[a] *Department of Chemistry, Korea Advanced Institute of Science and Technology (KAIST), Daejeon 34141, Republic of Korea. E-mail: hyotcherl.ihee@kaist.ac.kr*
[b] *Center for Advanced Reaction Dynamics (CARD), Institute for Basic Science (IBS), Daejeon 34141, Republic of Korea*
† Both authors contributed equally to this work.

CDBP. This behavior has been attributed to its flexible molecular structure, which promotes ICT upon excitation.[32,33] While these findings highlight the photophysical tunability of CBP, they fall short of revealing how such structural relaxation dynamics impact charge separation, transport, and recombination processes. Recent transient absorption (TA) studies involving CBP and its halogenated derivatives have revealed the variations in their triplet-state lifetimes.[34] However, they did not address the fundamental sequence of excited-state structural dynamics of CBP itself. Despite growing interest in organic electronic materials, the excited-state dynamics associated with ICT-driven structural changes—such as torsional planarization and the development of quinoidal resonance in the biphenyl core—remain poorly understood, particularly with respect to their spectroscopic signatures. In addition, the precise temporal relationship between electronic charge separation and subsequent structural reorganization has yet to be clarified. Gaining atomistic-level insight into this structural evolution of CBP is therefore crucial for linking molecular behavior to charge transport processes and ultimately guiding the rational design of high-performance organic electronic devices.

To gain mechanistic insight into the excited-state structural dynamics of CBP, we combined femtosecond transient absorption (fs-TA) spectroscopy, first-principles electronic structure calculations, and nonadiabatic molecular dynamics (NAMD) simulations. A variety of time-resolved techniques, including transient absorption, infrared, and Raman spectroscopies,[35–40] ultrafast electron diffraction (UED),[41–45] and time-resolved X-ray liquidography (TRXL),[46–53] have been employed to probe photoinduced structural changes. Among these techniques, fs-TA spectroscopy offers high temporal resolution and is highly sensitive to changes in excited-state populations and electronic configurations, making it particularly effective for capturing the earliest stages of excited-state dynamics. To complement our experimental analysis, we employed state-of-the-art NAMD simulations, which explicitly model the coupling between nuclear and electronic dynamics, providing direct atomistic insight into the structural evolution of the system. This combined approach enabled the identification of a sequence of photoinduced molecular rearrangements that govern the excited-state relaxation of CBP. Specifically: (i) following photoexcitation, a sub-picosecond ICT occurs from the carbazole to the biphenyl unit; (ii) this is followed by planarization of the biphenyl core; (iii) finally, a torsional twisting between the carbazole and biphenyl moieties takes place. These insights reveal the key molecular motions that govern CBP's excited state behavior, offering a blueprint for engineering advanced organic optoelectronic materials with enhanced performance and tailored functionalities.

Results and discussions

Optical properties of CBP

Fig. 1 shows the molecular structure of CBP, highlighting the two carbazole units and the biphenyl core. Typically, carbazole

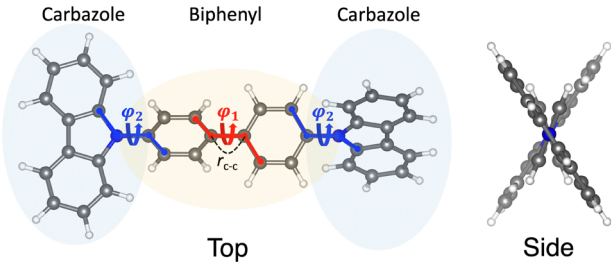

Fig. 1 Molecular structure of CBP in the ground state, shown from both top and side views. The dihedral angle between the phenyl rings in the biphenyl unit is denoted as φ_1 (highlighted in red), and the dihedral angles between the biphenyl and carbazoles are labeled as φ_2 (highlighted in blue). The black dotted line represents the C–C bond connecting the two phenyl rings (r_{c-c}). These dihedral angles and distances represent the relative rotational orientations of the aromatic rings, which play a crucial role in the electronic and structural properties of CBP.

serves as a strong electron donor, while biphenyl acts as an electron acceptor. To elucidate the photophysical properties of CBP, we measured the steady-state UV-visible absorption and emission spectra in various solvents: 2 solvents with low polarity (hexane and ethyl ether) and 3 solvents with high polarity (tetrahydrofuran (THF), dichloromethane (DCM) and acetonitrile (MeCN)) (see Fig. 2(a)). Notably, two prominent absorption peaks were observed at ~320 nm and ~290 nm, regardless of solvent polarity, reflecting the weak solvatochromic behavior of CBP.

To characterize the excited states associated with these two peaks, TD-DFT calculations were carried out. As shown in Fig. S1, TD-DFT calculations indicate that the broad absorption band at ~320 nm arises from electronic transitions to the S1 and S3 states, while the band at ~290 nm originates from transitions to the S5 and S6 states. The character of the excited states was investigated through natural transition orbital (NTO) analysis (Fig. S2), where the dominant NTO pairs and corresponding oscillator strengths for the bright states are presented. In particular, the NTOs corresponding to the S1 and S3 excitations mainly show (π,π^*) character transitions involving both the biphenyl core and the carbazole units in CBP. In contrast, the transitions to the S5 and S6 states predominantly show (π,π^*) character, localized on the carbazole moieties. To quantify the charge transfer (CT) and local excitation (LE) character of these bright excited states, the one-electron transition density matrix (1-TDM) analysis was performed, and the results are depicted in Fig. S3. This analysis reveals that the S1 and S3 transitions exhibit a hybrid LE–CT character, with LE within the carbazole moieties as the major component, CT from carbazole to the biphenyl core, and LE on the biphenyl core. In contrast, the S5 and S6 transitions are predominantly characterized by LE on the carbazole moieties, accounting for more than 95% of the character of these excited states. Taken together, the CT character of the low-lying excited states (S1 and S3) suggests a favorable propensity for electron–hole separation, supporting their potential role in charge transport processes.

To further support this theoretical prediction, we investigated the solvent-dependent photoluminescence behavior of

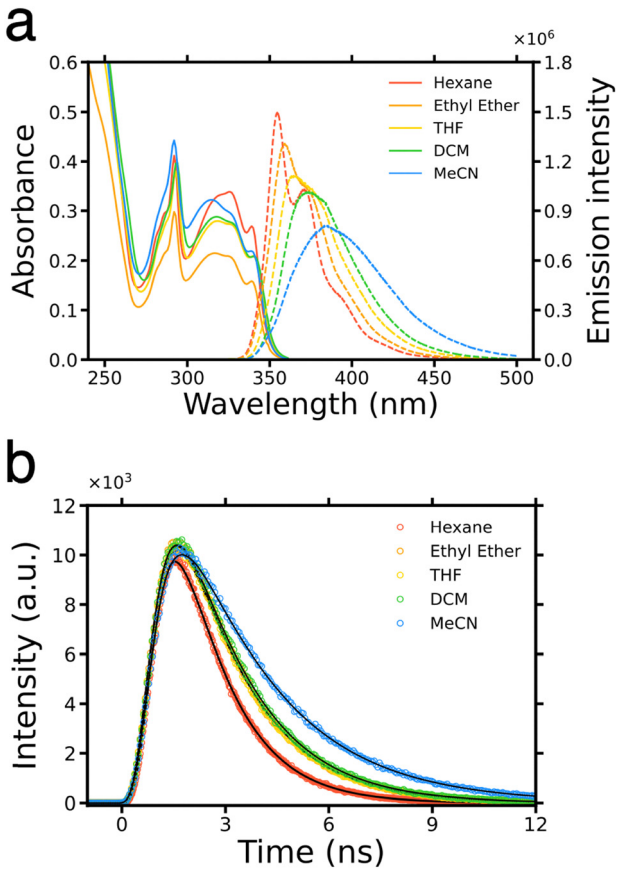

Fig. 2 UV-visible absorption and emission spectra and fluorescence decay profiles of CBP. (a) UV-visible absorption (solid lines) and emission (dotted lines) spectra of CBP, measured in various solvents. (b) Fluorescence decay profiles of CBP monitored in the emission peak maximum (λ_{ex} = 290 nm). The black solid lines are the fits with a single-exponential function. Fluorescence lifetimes are summarized in Table S2.

CBP. Experimental measurements reveal a pronounced red shift in the emission spectrum with increasing solvent polarity, consistent with enhanced stabilization of the CT state in polar environments. As shown in Fig. 2(a), increasing solvent polarity induces a red shift, a reduction in peak intensity, and a loss of vibronic structure. Additionally, the fluorescence lifetime of CBP increases from 1.30 ns in hexane to 2.59 ns in MeCN (Fig. 2(b) and Table S2), consistent with the progressive stabilization of the CT state in more polar environments. Furthermore, the Stokes shift varies significantly with respect to the solvent polarities, ranging from 1240 cm^{-1} in hexane to 3421 cm^{-1} in MeCN. In nonpolar solvents, CBP's emission closely resembles that of carbazole.[54] In contrast, large Stokes shifts are observed in highly polar solvents, suggesting that the red-shifted emission originates from a CT state.

This interpretation is further supported by the observed linear correlation between the Stokes shift and the solvent orientation polarizability Δf. Based on the slope obtained from the Lippert–mataga plot, the difference dipole moment ($\Delta\mu$) is determined to be 6.06 Debye (see Lippert–Mataga plot section in Fig. S4), indicating a substantial increase in dipole moment upon excitation, which is a common characteristic of CT nature. Our fluorescence measurement and Lippert–Mataga analyses reveal a nonzero dipole moment difference between the ground and excited states, indicating that symmetry-breaking charge transfer (SBCT) may occur in polar solvents, where solvent polarity lifts the degeneracy of CT states and induces symmetry-breaking CT. This observation finding is particularly noteworthy because CBP is a centrosymmetric molecule; if the delocalized CT state fully preserved this symmetry, the dipole moment difference would ideally vanish.[55,56] We therefore propose that, in polar solvents, SBCT from the carbazole to the biphenyl moiety may occur preferentially *via* a single carbazole unit, whereas in nonpolar environments the excited state remains predominantly delocalized and symmetric.

To track the structural evolution of CBP upon excitation, we optimized its geometry in both the S_0 and S_1 states, with the key geometrical parameters summarized in Table 1. Also, the potential energy surfaces (PES) of the S_0 and S_1 states were calculated, varying the φ_1 torsion angle and the C–C bond length (r_{c-c}) between the two phenyl rings in biphenyl, as defined in Fig. 1 and Fig. S5. At the stationary point of the S_0 state, CBP exhibits significant torsional distortion, with dihedral angles φ_1 = 137.2° and φ_2 = 125.4°, indicating a deviation from planarity. Conversely, the optimized S_1 structure adopts an almost planar biphenyl conformation, with φ_1 = 174.4°. In addition to φ_1, the φ_2 torsion angle connecting the biphenyl core to the carbazole unit also shows a notable difference of more than 10° between the optimized geometries of the S_0 and S_1 states, increasing from 125.4° to 136.5°. Additionally, in the minimum of the S_1 state, the r_{c-c} is shortened by 0.07 Å compared to the minimum of the S_0 state, although it remains longer (1.415 Å) than the C–C double bond length in ethylene (1.336 Å),[57] suggesting the onset of partial double-bond character. These results suggest that rotation of the φ_1 and φ_2 torsion angles, coupled with the contraction in the r_{c-c}, drive key structural changes occurring in the S_1 state. Having identified the key geometrical parameters driving the structural evolution from S_0 state to S_1 state, we performed time-resolved spectroscopy experiments and NAMD simulations, which are discussed in the following sections.

Femtosecond transient absorption (fs-TA) spectroscopy

To elucidate the detailed excited-state relaxation dynamics of CBP, we measured the fs-TA spectra in the same series of solvents with varying polarity investigated with static UV-visible absorption and emission measurements, upon excitation at 340 nm. As shown in Fig. 3, the fs-TA spectra of CBP in

Table 1 Structural parameters of optimized geometries of CBP in the S_0 and S_1 states, calculated using (TD)-DFT with the CAM-B3LYP functional and 6-31G(d,p) basis set

	r_{C-C}	r_{C-N}	φ_1	φ_2
S_0 (min)	1.482 Å	1.415 Å	137.2°	125.4°
S_1 (min)	1.415 Å	1.393 Å	174.4°	136.5°

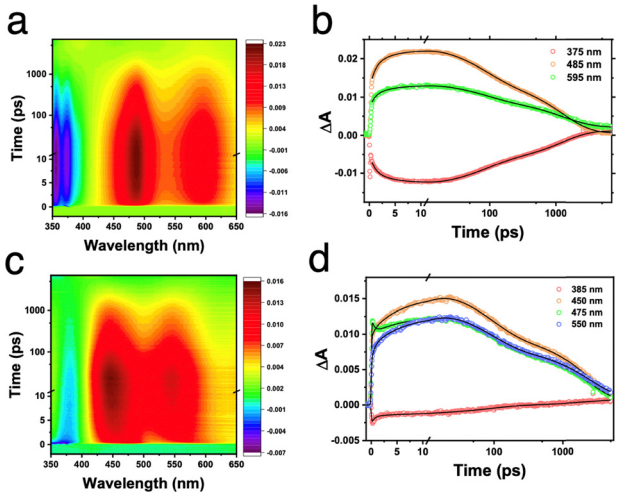

Fig. 3 Time-resolved TA spectra for CBP. (a), (c) Contour plots of TA spectra of CBP in *n*-hexane and MeCN, respectively. (b) Time profiles monitored at selected wavelengths (red: 375 nm, orange: 485 nm, and green: 595 nm) from the TA spectra measured in *n*-hexane. All decay profiles were well-expressed by a tetra-exponential function (0.90 ± 0.04 ps, 5.3 ± 0.2 ps, 79 ± 1 ps, and 1263 ± 7 ps). Fit curves are shown in black solid lines. (d) Time profiles monitored at selected wavelengths (red: 385 nm, orange: 450 nm, green: 475 nm, and blue: 550 nm) from the TA spectra measured in MeCN. All decay profiles were well-expressed by a tetra-exponential function (0.58 ± 0.02 ps, 7.2 ± 0.1 ps, 89 ± 1 ps, and 2500 ± 27 ps). Fit curves are shown in black solid lines.

hexane, a nonpolar solvent, are characterized by a negative signal around ~360 nm due to the stimulated emission (SE) and two positive signals around ~470 and ~600 nm corresponding to the excited-state absorption (ESA). At early delay times (<10 ps), both SE and ESA signals increase in intensity without significant spectral shifts, followed by a gradual decay of all signals at later times (>10 ps). To quantify the overall kinetics of CBP in the excited state, the time evolution of the TA spectra at specific wavelengths in hexane was analyzed and well-expressed by tetra-exponential functions with shared time constants of 0.9 ± 0.1 ps, 5.3 ± 0.2 ps, 79 ± 1 ps, and 1263 ± 7 ps. Similar spectral features and kinetic behavior were observed in ethyl ether and DCM, and all decay profiles were also well-described by a tetra-exponential function (Fig. S6 and S7). In contrast, the fs-TA spectra measured in MeCN exhibit a negative signal around 375 nm attributed to SE, along with two positive signals around 450 and 550 nm corresponding to the ESA. Unlike in hexane, early-time TA signals in MeCN show significant red and blue shifts in the negative and positive bands. Global fitting of the decay profiles across multiple wavelengths of the TA spectra measured in MeCN yielded a tetra-exponential model with shared time constants of 0.6 ± 0.1 ps, 7.2 ± 0.1 ps, 89 ± 1 ps, and 2500 ± 7 ps. In Table 2, we list the time constants determined by global analysis of TA data of CBP in various solvents.

Notably, in a highly polar solvent, such as MeCN, the ESA band at early delay times is significantly blue shifted. This shift correlates with the earliest kinetic component (τ_1 in Table 2), which shows an apparent dependence on solvent polarity,

Table 2 Time constants obtained from fs-TA experiments. All time constants are reported in picoseconds (ps) time scale

	Hexane	Ethyl ether	DCM	MeCN	Triacetin
τ_1	0.90 ± 0.04	0.97 ± 0.10	0.75 ± 0.07	0.58 ± 0.02	0.92 ± 0.05
τ_2	5.3 ± 0.2	7.8 ± 0.3	8.9 ± 0.1	7.2 ± 0.1	20.5 ± 0.9
τ_3	79 ± 1	64 ± 1	104 ± 1	89 ± 1	241 ± 9
τ_4	1263 ± 7	1718 ± 15	1836 ± 1	2500 ± 27	1571 ± 15

consistent with the behavior of many systems exhibiting charge-transfer dynamics in the excited state, as described by the following relationship:

$$k_{CT} \cong \tau_s^{-1}$$

where k_{CT} is the CT rate constant and τ_s is the time constant associated with solvent reorganization.[58–63] Notably, the τ_1 of 0.6 ps obtained from the fs-TA spectrum in MeCN is close to the previously reported τ_s value of MeCN (0.4–0.9 ps).[64] Therefore, we attribute τ_1 to a polarity-dependent CT process between the carbazole and biphenyl units, resulting in relaxation into a CT state.

Meanwhile, as shown in Table 2, τ_2 and τ_3 exhibit no dependence on solvent polarity. It is worth recalling that our TD-DFT calculations indicate that the twisted conformation of CBP in the ground state undergoes planarization of the biphenyl moiety in the excited state. Additionally, the CT process in CBP results in a charge-separated excited state, in which the biphenyl unit bears excess electronic density. The resulting biphenyl radical anion ($BP^{\bullet -}$) likely adopts a planar, quinoidal geometry, in contrast to the twisted conformation of neutral biphenyl in the ground state.[65] Therefore, we propose that τ_2 and τ_3 are associated with the structural reorganization process of CBP. Since such structural changes require a certain degree of conformational flexibility, a critical assessment of this assignment is to examine the behavior of these time constants in solvents of varying viscosity, where increased viscosity is expected to restrict molecular motion and thereby slow down or hinder structural relaxation. To experimentally assess this effect, we measured the fs-TA spectrum in triacetin, a solvent with similar polarity and significantly higher viscosity than DCM (17.4 cP for triacetin, 0.41 cP for DCM). As shown in Table 2 and Fig. S8, the time constants τ_2 and τ_3, obtained in triacetin, are significantly affected by the solvent viscosity, while the spectral features remain similar to those observed in DCM. Specifically, τ_2 and τ_3 measured in triacetin are 20.5 ps and 241 ps, respectively, compared to 8.9 ps and 104 ps in DCM. This clearly highlights the slower structural relaxation resulting from increased solvent viscosity. The viscosity-dependent dynamics of CBP strongly support the assignment of these time constants (τ_2 and τ_3) to structural relaxation processes, such as the planarization of the φ_1 angle and the twisting of the φ_2 angle. Therefore, we tentatively attribute τ_2 to the planarization of the biphenyl moiety *via* rotation of the φ_1 angle, and τ_3 to the twisting between the carbazole and biphenyl, through rotation of the φ_2 angle, respectively. As we will discuss later, this assignment is further supported by NAMD

simulations, which reveal a sequential structural evolution consistent with these processes.

Finally, as shown in Table 2 and Table S2, τ_4 shows a strong correlation with the fluorescence lifetime, and its relatively long timescale further supports its assignment to radiative decay from the structurally relaxed CT state back to the ground state.

Excited state molecular dynamics simulations

To investigate the structural dynamics of CBP upon excitation, NAMD simulations based on the surface hopping framework were performed. Initial conditions were generated from a Wigner distribution around the ground-state minimum, and excited states were stochastically selected to match the second absorption band observed experimentally at ~290 nm (Fig. S9). Full computational details are reported in the Nonadiabatic molecular dynamics simulations section in computational details. The resulting time-resolved adiabatic state populations are shown in Fig. S10. Rapid internal conversion (IC) from higher singlet states (S_n) to the S_1 state occurred within 100 fs in 60% of the trajectories, and over 80% within 300 fs. Consequently, the structural dynamics following photoexcitation are expected to primarily evolve on the S_1 state PES, and our analysis therefore focused on the processes taking place in the S_1 state.

Fig. 4 presents the time-dependent changes of the φ_1 and φ_2 torsion angles during the NAMD simulations. The φ_1 angle, which is approximately 140° in the Franck–Condon region, gradually evolves toward a planar configuration (~180°) within 1 ps. Not only φ_1, but also the time evolution of the φ_2 angle shows oscillations with a period like that of φ_1, with different amplitudes. Notably, at 1 ps, the averaged φ_2 angle remains at 125°, deviating from the value observed in the fully relaxed geometry (φ_2 = 136.5°) in the S_1 state, likely due to residual vibrational energy along the φ_2 torsional mode during S_1 state dynamics. These results suggest that, following the initial planarization of the biphenyl moiety, further structural relaxation involving twisting of the φ_2 angles proceeds on a much slower timescale. Additionally, as depicted in Fig. S11, the r_{c-c} value exhibits notable variations. Initially, the C–C bond lengths within each phenyl ring were 1.39 Å, while the r_{c-c} connecting the two phenyl rings measured 1.50 Å. During the simulations, the central C–C bond (R1) shortened, the adjacent C–C bonds (R2) elongated, while the other C–C bonds (R3) remained unchanged (see top panel of Fig. S11 for the definition of the C–C bond types). In the first 150 fs, R1 and R2 values converged to nearly identical distances of 1.45 Å, while R3 did not show any alternation of bond length during 1 ps. Therefore, conjugation between the two phenyl rings is established at an early stage of the simulation, while full planarization of the biphenyl unit, particularly involving the φ_1 angle, proceeds more gradually during the relaxation process, followed by the slower relaxation of the φ_2 angle. The NAMD simulations support our interpretation that τ_2 and τ_3 are associated with the planarization of the biphenyl moiety *via* rotation of the φ_1 angle and the twisting between the carbazole and biphenyl units *via* rotation of the φ_2 angles, respectively.

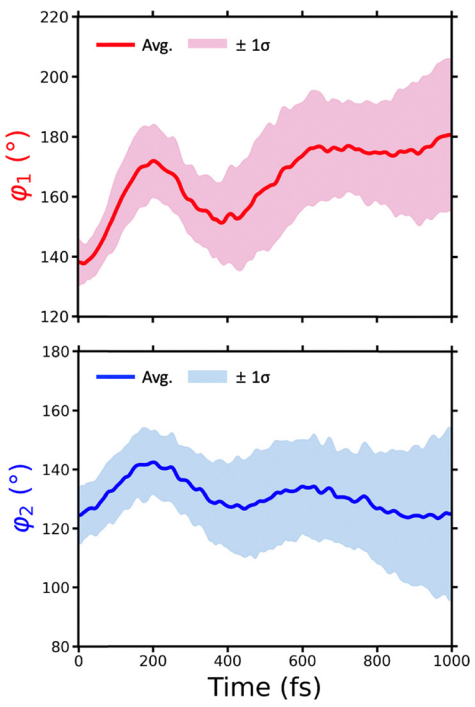

Fig. 4 The time evolution of two representative dihedral angles, φ_1 (red) and φ_2 (blue), up to 1 ps. The averaged values of each parameter (solid lines) are shown along with $\pm 1\sigma$ standard deviations (the shaded area). The φ_2 value was averaged for two φ_2 angles.

To further investigate the vibrational modes related to the structural dynamics of CBP in the excited state, normal mode analysis (NMA) was performed along the surface hopping trajectories. Fig. 5 presents the activity of the dominant normal modes (R_{act}), along with their corresponding normal mode vectors. Notably, the ν_{14} and ν_{70} modes, associated with torsion along the φ_1 angle, and the ν_3 and ν_{64} modes, related to torsion around the φ_2 angles, were found to be active throughout the simulations. At early times, the ν_{14} and ν_{70} modes exhibited high R_{act} values, whereas the ν_3 and ν_{64} modes showed low R_{act} values. As the simulation progressed, this behavior inverted, with R_{act} for ν_{14} and ν_{70} gradually decreasing and that for ν_3 and ν_{64} increasing. This trend suggests a dynamic redistribution of vibrational energy. Initially, torsional modes associated with the φ_1 angle are primarily activated, followed by a gradual increase of the R_{act} for vibrational modes related to φ_2 twisting as biphenyl planarization progresses, as discussed above. Therefore, our NAMD simulation suggests that intramolecular vibrational energy redistribution (IVR) between the ν_3 and ν_{14} modes, occurring in the S_1 state, facilitates the further relaxation of the φ_2 angles, occurring at a slower time scale than planarization of biphenyl through the rotation of the φ_1 angle.

Finally, it is worth noting that no transitions from the S_1 to the S_0 state were observed in any trajectory throughout the NAMD simulations, suggesting that radiative decay may be preferred over non-radiative decay. To further confirm this, the radiative rate constant (k_r) and non-radiative decay rate (k_{nr}) were calculated using the Adiabatic Hessian (AH) approximation within

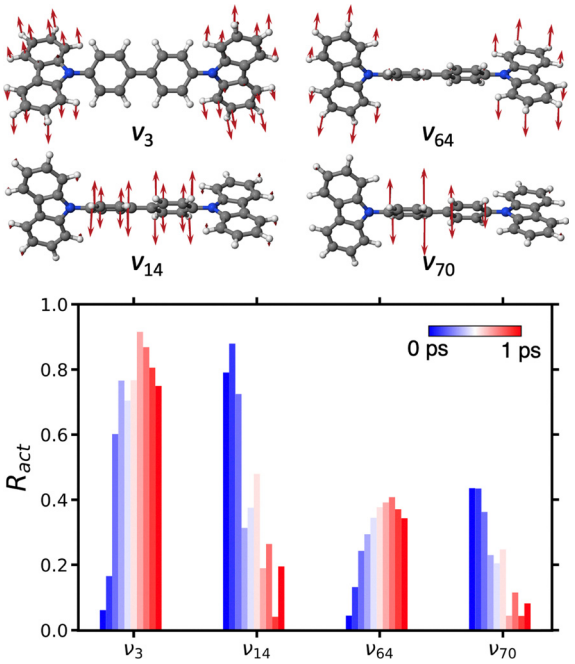

Fig. 5 Normal mode activity (R_{act}) of selected vibrational modes shown at 100 fs intervals. Among all normal modes of CBP in the S_1 state, only those exhibiting R_{act} values exceeding 0.3 at least once within these intervals were shown. The corresponding normal mode displacement vectors are also illustrated.

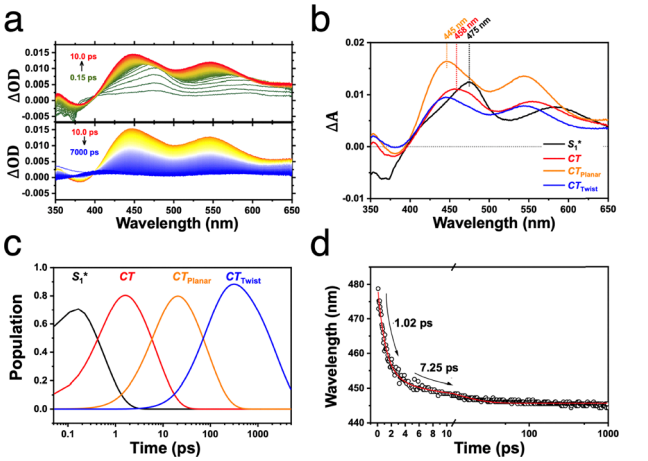

Fig. 6 Kinetic model analysis for TA spectra of CBP. (a) TA spectra of CBP measured in MeCN. (b) Evolution-associated spectra (EAS) corresponding to S_1^*, CT, CT_{Planar}, and CT_{Twist} states. (c) Population changes for four states, S_1^*, CT, CT_{Planar}, and CT_{Twist}, for CBP in MeCN. (d) Spectral relaxation for CBP measured in MeCN. The spectral relaxation is satisfactorily fitted by a biexponential function with two time constants of 1.0 ± 0.1 ps and 7.2 ± 0.6 ps. The fitting curve is shown as a red solid line.

the Fermi's Golden Rule framework, as detailed in the Calculation of rate constants section. Our calculations yielded the k_r value of $6.92 \times 10^8\ s^{-1}$ and k_{nr} value of $5.74 \times 10^6\ s^{-1}$. The k_r value, greater than calculated k_{nr} value over 100 times, confirms that relaxation to the ground state occurs predominantly *via* radiative decay. This result implies that the conical intersection between the S_0 and S_1 states lies in a high-energy region that is most likely inaccessible under our experimental conditions. These observations align with the high emission quantum yield of CBP (see Table S2), further supporting the dominance of radiative decay pathways.

TA spectra analysis with a kinetic model

To further elucidate the structural dynamics induced by CT, we carried out the kinetic analysis of the fs-TA spectra of CBP using a sequential kinetic model. Based on the assignment of the time constants in the Femtosecond transient absorption (fs-TA) spectroscopy section, we carried out a kinetic analysis using the following sequential reaction scheme:

$$S_0 \xrightarrow{h\nu} S_1^* \xrightarrow{\tau_1} CT \xrightarrow{\tau_2} CT_{Planar} \xrightarrow{\tau_3} CT_{Twist} \xrightarrow{\tau_4} S_0$$

CT refers to a CT state without geometrical relaxation, CT_{Planar} denotes a CT state planarized along the φ_1 angle, and CT_{Twist} corresponds to a twisted CT state involving the twisting of the φ_2 angles. As a result, we found that the sequential kinetic model well describes the excited-state dynamics of CBP in both non-polar and highly polar solvents. Fig. 6 shows the evolution-associated spectra (EAS) and the relative population of the respective species, S_1^*, CT, CT_{Planar}, and CT_{Twist}. As shown in Fig. 6(b), the CT process in MeCN, occurring with a time constant of 0.6 ps, induces a blue shift of the ESA from 475 to 458 nm.

Also, planarization of the biphenyl moiety, occurring with a time constant of 7.1 ps, further contributes to a blue shift of ESA from 458 to 445 nm. In contrast, twisting of the φ_2 angles between the carbazole and biphenyl units, which takes place on a slower timescale of 90 ps, does not result in any spectral shift. These observations suggest that the spectral shifts observed in the TA spectra primarily arise from the solvent reorganization associated with CT and the planarization of the biphenyl moiety. The absence of a spectral shift due to twisting between the carbazole and biphenyl moieties *via* rotation of the φ_2 angles is likely due to the relatively small and slow torsional motion between these carbazole and biphenyl moieties. In fact, in the S_1 state, the calculated frequency of the ν_3 mode is significantly lower than that of the ν_{14} mode (see Table S1). Since lower-frequency modes correspond to slower vibrational motions, our calculations indicate that the carbazole–biphenyl twisting through relaxation of the φ_2 angles proceeds more slowly than the planarization of the biphenyl unit.

Additionally, the maximum wavelength of the fs-TA spectra for CBP, measured in MeCN, was plotted as a function of delay time in Fig. 6(d). The spectral relaxation is well described by a biexponential fit with two time constants: 1.0 ± 0.1 ps and 7.2 ± 0.6 ps. Notably, as shown in Fig. 6, CBP in MeCN exhibits a relatively slow spectral relaxation component (~1.0 ps), which is notably longer than the ~0.6 ps timescale typically associated with dipolar solvent relaxation in CT processes. This difference suggests the presence of an additional relaxation mechanism beyond simple solvation. As discussed above, our NAMD simulations indicate that relaxation to the S_1 state occurs more rapidly than the establishment of conjugation

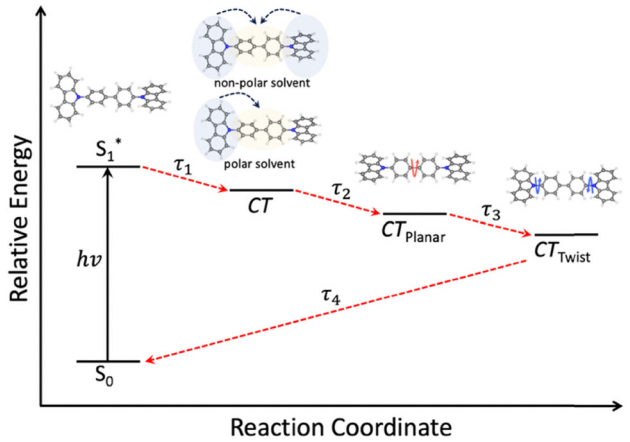

Fig. 7 Schematic representation of the excited-state dynamics of the CBP molecule. Following photoexcitation, a CT from the carbazole to the biphenyl moiety occurs with a time constant τ_1. This is followed by planarization of the biphenyl unit, which facilitates relaxation into the CT_{Planar} state, occurring with a time constant τ_2. Subsequent twisting around the φ_2 angles leads to the formation of the CT_{Twist} with a time constant τ_3. Finally, the system relaxes back to the ground state with a time constant τ_4. Table 2 summarizes the time constants measured across a diverse range of solvents.

between the two phenyl rings (biphenyl planarization). This suggests that the discrepancy between the spectral shift analysis and the kinetic analysis of the TA spectra likely arises from a discrepancy in timescales, where an initial change in electronic structure driven by CT occurs earlier than the biphenyl planarization in the excited state. Recently, Yoneda *et al.* showed that upon photoexcitation, cyclooctatetraene (COT) derivatives undergo an initial change in electronic structure, leading to excited-state aromatization that in turn triggers conformational reorganization.[66] In this respect, we suggest that the spectral relaxation dynamics occurring on the ~1 ps timescale are associated with the formation of a quinoidal structure, which is a resonance form of the biphenyl moiety, induced by rapid CT. Finally, we note that our current approach cannot directly resolve SBCT dynamics under polar conditions. Future studies employing time-resolved infrared (TR-IR) or time-resolved fluorescence spectroscopy could provide deeper insights into the conformational dynamics, the evolution of quinoidal character in the excited state, and any associated SBCT processes.

Conclusions

The present study provides a comprehensive picture of the excited-state dynamics in CBP, achieved by synergistically integrating fs-TA spectroscopy with NAMD simulations. First, employing steady-state UV-visible, emission, and TCSPC measurements, together with electronic structure calculations, we explored the detailed properties of the excited states. To further investigate the structural relaxation dynamics of CBP in the excited state, we conducted fs-TA experiments in a variety of solvents with different polarities and viscosities. As shown in Fig. 7, our findings show that photoinduced CT in CBP serves as a structural trigger, initiating a cascade of electronic conjugation in the biphenyl moiety and conformational relaxation *via* rotation of φ_1 and φ_2 angles. Specifically, following CT from the carbazole donor to the biphenyl acceptor, the biphenyl undergoes planarization through rotation of φ_1, with a time constant of ~7 ps. The subsequent twisting motion between the carbazole and biphenyl units, mediated by rotation around φ_2, occurs on a much slower timescale of ~90 ps. The sequence of structural motions is further supported by NAMD simulations, which clearly show that biphenyl planarization occurs much faster than the twisting between the carbazole and biphenyl units. Additionally, we confirmed that IVR between normal modes associated with the two torsional angles drives the relaxation dynamics of CBP. These insights uncover the critical molecular motions that dictate CBP's excited-state behavior, providing a foundation for the rational design of advanced organic optoelectronic materials with improved performance and customized functionalities. In conclusion, judicious substitution at the biphenyl core or the carbazole units, aimed at controlling the excited-state evolution of dihedral angles, could serve as an effective strategy to modulate excited-state lifetimes, enhance radiative quantum yields, optimize electron–hole separation, and improve charge transport properties.

Experimental details

Sample details

The 4,4′-bis(*N*-carbazolyl)-1,1′-biphenyl (CBP) was purchased from Tokyo Chemical Industry (TCI) Co., Ltd, and *n*-hexane, ethyl ether, dichloromethane, triacetin, and acetonitrile were purchased from Sigma-Aldrich. All chemicals were used without further purification.

Steady-state spectroscopy

Steady-state absorption and emission spectra were measured using a UV-Vis-NIR scanning spectrophotometer (Agilent Technologies, Cary 5000) and a fluorescence spectrophotometer (Horiba, FluoroMax), respectively. Time-correlated single photon counting (TCSPC) experiments were conducted using a Fluorescence lifetime spectrometer (Hamamatsu Photonics, Quantaurus-Tau). All steady-state spectroscopy measurements were conducted under concentrations of 10 μM.

Femtosecond transient absorption spectroscopy

Femtosecond transient absorption (fs-TA) spectra of CBP in various solvents were measured using a TA spectroscopy system (Ultrafast Systems, Helios) coupled with a Ti:sapphire femtosecond laser system. The output pulses at a wavelength of 800 nm from a Ti:sapphire amplified laser (Coherent, Astrella, 34 fs, 1 kHz) were split to generate the pump and probe pulses. The wavelength of laser pulses in the pump arm was converted to 340 nm using an optical parametric amplifier (Light Conversion, TOPAS prime). The other part of the fundamental laser

pulses was directed to a CaF_2 window to generate a white light continuum for the probe beam. This white light passed through a 2-mm pathlength sample cell, and the transmitted light was collected by a CCD detector integrated into the transient absorption system. The pump pulse was modulated by a mechanical chopper synchronized to one-half (500 Hz) of the laser repetition rate, resulting in a pair of spectra with and without the pump, from which an absorption change induced by the pump pulse was quantified. The pump pulse intensity was adjusted to 47.8 μJ mm^{-2} using a continuously variable neutral density filter. The optical delay between pump and probe beams was precisely controlled to achieve the desired time delay. Fs-TA experiments were conducted at a concentration of 250 μM, where no aggregation was observed (see Fig. S12).

Computational details

Electronic structure calculations

To begin, we optimized the geometry of CBP in its ground singlet state (S_0) using the CAM-B3LYP/6-31G(d,p) level of theory,[67–69] incorporating the conductor-like polarizable continuum model (C-PCM) to account for the solvent effect of acetonitrile.[70] The optimized structure showed no imaginary frequencies, confirming that it corresponds to a stationary point on the S_0 surface. Using this geometry as a reference, excitation energies, natural transition orbitals (NTOs), and oscillator strengths for each excited state were calculated using time-dependent density functional theory (TD-DFT) with the Tamm–Dancoff approximation (TDA).[71] To quantitatively evaluate the CT and LE characters between the carbazole and biphenyl moieties, one-electron transition density matrix (1-TDM) analysis was performed. The CBP molecule was partitioned into two fragments: the biphenyl core and the two carbazole units. Based on this partitioning, a 2×2 Ω matrix was constructed, where the diagonal elements represent LE contributions within each fragment, and the off-diagonal elements correspond to CT contributions between fragments. Additionally, two-dimensional PES scans were performed for the S_0 and S_1 states with respect to the φ_1 angle and the r_{c-c} between the two phenyl rings, as shown in Fig. S5. All DFT and TD-DFT calculations were performed using the ORCA 5.0.4 program,[72,73] and the 1-TDM analysis was conducted using the TheoDORE 3.0 package.[74,75]

Nonadiabatic molecular dynamics simulations

To investigate the detailed structural dynamics of CBP in the excited state, we performed NAMD simulations using a trajectory surface hopping framework. The simulations employed the CAM-B3LYP functional and the 6-31G(d,p) basis set, and the polar environment of acetonitrile was modeled using C-PCM with an equilibrium solvent model, in which the solvent responds to the excited-state charge distribution. While this approach captures the overall solvent stabilization, it does not explicitly account for anisotropic solvent effects that can influence SBCT, which is a known limitation of the C-PCM framework. For the initial conditions, 200 geometries were sampled from a harmonic Wigner distribution, using the ground-state optimized geometry and its harmonic frequencies. Initial excited states were then stochastically selected based on calculated excitation energies and oscillator strengths within the 4.15–4.55 eV range, corresponding to the second absorption peak observed at ~290 nm (4.25 eV) in the experimental spectrum. These trajectories were launched from the selected excited states and propagated using the velocity-Verlet algorithm with a time step of 0.5 fs for a total duration of 1 ps. We note that all trajectories successfully propagated to 1 ps without premature termination. To mitigate the well-known overcoherence problem in surface hopping simulation, an energy-difference-based decoherence correction (EDC) was applied using a decoherence parameter of 0.1 Hartree, as proposed by Granucci *et al.*[76] Hopping probabilities between electronic states were calculated using the local diabatization scheme, where non-adiabatic coupling vectors are approximated *via* overlap matrices.[77] Upon electronic transitions, nuclear velocities were rescaled along the direction of the velocity vector to preserve the total energy. Normal mode analysis (NMA) was conducted using a built-in Python script implemented in the SHARC code.[78] All NAMD simulations were performed using the SHARC 3.0/ORCA 5.0.4 interface.[79,80]

Calculation of rate constants

The radiative rate constant (k_r) and non-radiative rate constant (k_{nr}) were calculated using the Adiabatic Hessian (AH) approach. Briefly, the AH approach expands the minima of the PES for the S_0 and S_1 states within harmonic approximation, based on the calculated normal mode information at the stationary points of both states.[81] We chose the AH approach over vertical methods due to the significant structural distortions in the excited state. To calculate k_r, we integrated the calculated emission spectrum for the energy. Non-radiative rate constants (k_{nr}) were calculated based on Fermi's Golden Rule (FGR) framework, using the non-adiabatic coupling matrix element (NACME) and the vertical energy gap between the two electronic states, both evaluated at the stationary point of the S_1 state. For the rate constant calculations, the FCCLASSES 3.0 package was employed.[82]

Author contributions

Conceptualization: J. C., D. I., H. I.; data curation: J. C., D. I., J. H. L.; formal analysis: J. C., D. I., J. H. L.; funding acquisition: H. I.; investigation: J. C., D. I., J. H. L., A. S., H. I.; methodology: J. C., D. I., J. H. L.; software: D. I., J. H. L., A. S.; supervision: H. I.; validation: J. C., D. I.; visualization: J. C., D. I., J. H. L.; writing – original draft: J. C., D. I.; writing – review & editing: J. C., D. I., A. S., H. I.

Conflicts of interest

The authors declare no conflict of interests.

Data availability

The data supporting this article have been included as part of the supplementary information (SI). Supplementary information: figures and tables for the experimental and theoretical datas. See DOI: **https://doi.org/10.1039/d5cp03464g**.

Acknowledgements

This work was supported by the Institute for Basic Science (IBS-R033). We thank the IBS Research Solution Center (RSC) for supporting computational resources. D. I. and A. S. gratefully acknowledge Professor Javier Cerezo for his valuable insights and stimulating discussions.

Notes and references

1 H. Li, W. Shi, J. Song, H.-J. Jang, J. Dailey, J. Yu and H. E. Katz, *Chem. Rev.*, 2019, **119**, 3–35.
2 W. Park, J. Shen, S. Lee, P. Piecuch, T. Joo, M. Filatov(Gulak) and C. H. Choi, *J. Phys. Chem. C*, 2022, **126**, 14976–14985.
3 H. Chen, W. Zhang, M. Li, G. He and X. Guo, *Chem. Rev.*, 2020, **120**, 2879–2949.
4 S. R. Forrest and M. E. Thompson, *Chem. Rev.*, 2007, **107**, 923–925.
5 A. W. Hains, Z. Liang, M. A. Woodhouse and B. A. Gregg, *Chem. Rev.*, 2010, **110**, 6689–6735.
6 A. D. Xia, S. Wada and H. Tashiro, *Appl. Phys. Lett.*, 1998, **73**, 1323–1325.
7 G. Zhang, F. R. Lin, F. Qi, T. Heumüller, A. Distler, H.-J. Egelhaaf, N. Li, P. C. Y. Chow, C. J. Brabec, A. K.-Y. Jen and H.-L. Yip, *Chem. Rev.*, 2022, **122**, 14180–14274.
8 M. Bendikov, F. Wudl and D. F. Perepichka, *Chem. Rev.*, 2004, **104**, 4891–4946.
9 K. A. Mazzio and C. K. Luscombe, *Chem. Soc. Rev.*, 2015, **44**, 78–90.
10 H. Bronstein, C. B. Nielsen, B. C. Schroeder and I. McCulloch, *Nat. Rev. Chem.*, 2020, **4**, 66–77.
11 E. K. Lee, M. Y. Lee, C. H. Park, H. R. Lee and J. H. Oh, *Adv. Mater.*, 2017, **29**, 1703638.
12 S. Giannini and J. Blumberger, *Acc. Chem. Res.*, 2022, **55**, 819–830.
13 O. P. Dimitriev, *Chem. Rev.*, 2022, **122**, 8487–8593.
14 Y. Wei, S. Samori, S. Tojo, M. Fujitsuka, J.-S. Lin, C.-T. Chen and T. Majima, *J. Am. Chem. Soc.*, 2009, **131**, 6698–6707.
15 F. Coppola, P. Cimino, A. Petrone and N. Rega, *J. Phys. Chem. A*, 2024, **128**, 1620–1633.
16 M. Zharnikov, *Acc. Chem. Res.*, 2020, **53**, 2975–2984.
17 F. Coppola, M. Hussain, J. Zhao, A. M. El-Zohry and M. Pastore, *J. Phys. Chem. C*, 2024, **128**, 11998–12009.
18 C. Kim, T. W. Kim, S. Kim, I. Oh, H. Wonneberger, K. Yoon, M. Kwak, J. Kim, J. Kim, C. Li, K. Müllen and H. Ihee, *J. Phys. Chem. C*, 2020, **124**, 22993–23003.
19 S. Loser, S. J. Lou, B. M. Savoie, C. J. Bruns, A. Timalsina, M. J. Leonardi, J. Smith, T. Harschneck, R. Turrisi, N. Zhou, C. L. Stern, A. A. Sarjeant, A. Facchetti, R. P. H. Chang, S. I. Stupp, M. A. Ratner, L. X. Chen and T. J. Marks, *J. Mater. Chem. A*, 2017, **5**, 9217–9232.
20 C. S. Ponseca, P. Chábera, J. Uhlig, P. Persson and V. Sundström, *Chem. Rev.*, 2017, **117**, 10940–11024.
21 A. Segalina, J. Cerezo, G. Prampolini, F. Santoro and M. Pastore, *J. Chem. Theory Comput.*, 2020, **16**, 7061–7077.
22 A. Segalina, X. Assfeld, A. Monari and M. Pastore, *J. Phys. Chem. C*, 2019, **123**, 6427–6437.
23 A. Segalina, D. Aranda, J. A. Green, V. Cristino, S. Caramori, G. Prampolini, M. Pastore and F. Santoro, *J. Chem. Theory Comput.*, 2022, **18**, 3718–3736.
24 P. Schrögel, A. Tomkevičienė, P. Strohriegl, S. T. Hoffmann, A. Köhler and C. Lennartz, *J. Mater. Chem.*, 2011, **21**, 2266–2273.
25 Z. Yu, H. Feng, J. Zhang, S. Liu, Y. Zhao, L. Zhang and W. Xie, *J. Mater. Chem. C*, 2019, **7**, 9301–9307.
26 D. Y. Kondakov, W. C. Lenhart and W. F. Nichols, *J. Appl. Phys.*, 2007, **101**, 024512.
27 T. Yamada, F. Suzuki, A. Goto, T. Sato, K. Tanaka and H. Kaji, *Org. Electron.*, 2011, **12**, 169–178.
28 R. Newcomb, J. S. Bangsund, K. W. Hershey, D. C. K. Rathwell, H.-Y. Na, J.-H. Jeon, P. Trefonas and R. J. Holmes, *Appl. Phys. Lett.*, 2020, **116**, 063302.
29 A. A. Rudnick, S. Bagnich, D. Wagner, S. Athanasopoulos, P. Strohriegl and A. Köhler, *J. Chem. Phys.*, 2016, **144**, 214906.
30 H.-Z. Gao, *Synth. Met.*, 2010, **160**, 2104–2108.
31 D. Bhattacharyya, P. Dhar, Y. Liu, P. I. Djurovich, M. E. Thompson and A. V. Benderskii, *ACS Appl. Mater. Interfaces*, 2020, **12**, 26515–26524.
32 S. A. Bagnich, S. Athanasopoulos, A. Rudnick, P. Schroegel, I. Bauer, N. C. Greenham, P. Strohriegl and A. Köhler, *J. Phys. Chem. C*, 2015, **119**, 2380–2387.
33 S. T. Hoffmann, P. Schrögel, M. Rothmann, R. Q. Albuquerque, P. Strohriegl and A. Köhler, *J. Phys. Chem. B*, 2011, **115**, 414–421.
34 Z. Jiang, Y. Yang, Y. Liu, T. Guan, C. Qin and Y. Liu, *Spectrochim. Acta, Part A*, 2025, **329**, 125554.
35 S. Kim, D.-S. Ahn, M. Ahn, K.-R. Wee, J. Choi and H. Ihee, *Phys. Chem. Chem. Phys.*, 2020, **22**, 28440–28447.
36 A. Vlček, H. Kvapilová, M. Towrie and S. Záliš, *Acc. Chem. Res.*, 2015, **48**, 868–876.
37 C. Lu, K. Honda and M. Fujitsuka, *J. Phys. Chem. A*, 2024, **128**, 9869–9875.
38 S. Kim, J. Choi, D. W. Cho, M. Ahn, S. Eom, J. Kim, K.-R. Wee and H. Ihee, *Chem. Sci.*, 2022, **13**, 3809–3818.
39 H. Kuramochi, T. Tsutsumi, K. Saita, Z. Wei, M. Osawa, P. Kumar, L. Liu, S. Takeuchi, T. Taketsugu and T. Tahara, *Nat. Chem.*, 2024, **16**, 22–27.
40 M. Maiuri, M. Garavelli and G. Cerullo, *J. Am. Chem. Soc.*, 2020, **142**, 3–15.
41 Y. Lee, K. Y. Oang, D. Kim and H. Ihee, *Struct. Dyn.*, 2024, **11**, 031301.
42 J. Heo, D. Kim, A. Segalina, H. Ki, D.-S. Ahn, S. Lee, J. Kim, Y. Cha, K. W. Lee, J. Yang, J. P. F. Nunes, X. Wang and H. Ihee, *Nature*, 2024, **625**, 710–714.

43 T. Wang, H. Jiang, C. Jin, X. Zou, P. Zhu, T. Jiang, F. He and D. D. Xiang, *J. Chem. Phys.*, 2025, **162**, 184201.
44 J. Cao, H. Ihee and A. H. Zewail, *Chem. Phys. Lett.*, 1998, **290**, 1–8.
45 M. Centurion, T. J. A. Wolf and J. Yang, *Annu. Rev. Phys. Chem.*, 2022, **73**, 21–42.
46 J. H. Lee, T. K. Kim, J. Kim, Q. Kong, M. Cammarata, M. Lorenc, M. Wulff and H. Ihee, *J. Am. Chem. Soc.*, 2008, **130**, 5834–5835.
47 N. E. Powers-Riggs, B. O. Birgisson, S. L. Raj, E. Biasin, P. Lenzen, D. B. Zederkof, M. Haubro, D. K. V. Tveiten, R. W. Hartsock, T. B. Van Driel, K. Kunnus, M. Chollet, J. S. Robinson, S. Nelson, R. Forbes, K. Haldrup, K. S. Pedersen, G. Levi, A. O. Dohn, H. Jónsson, K. B. Møller, A. Natan, M. M. Nielsen and K. J. Gaffney, *J. Am. Chem. Soc.*, 2024, **146**, 13962–13973.
48 K. J. Gaffney and H. N. Chapman, *Science*, 2007, **316**, 1444–1448.
49 J. G. Kim, T. W. Kim, J. Kim and H. Ihee, *Acc. Chem. Res.*, 2015, **48**, 2200–2208.
50 E. H. Choi, Y. Lee, J. Heo and H. Ihee, *Chem. Sci.*, 2022, **13**, 8457–8490.
51 V. Markmann, J. Pan, B. L. Hansen, M. L. Haubro, A. Nimmrich, P. Lenzen, M. Levantino, T. Katayama, S. Adachi, S. Gorski-Bilke, F. Temps, A. O. Dohn, K. B. Møller, M. M. Nielsen and K. Haldrup, *Chem. Sci.*, 2024, **15**, 11391–11401.
52 K. H. Kim, J. H. Lee, J. Kim, S. Nozawa, T. Sato, A. Tomita, K. Ichiyanagi, H. Ki, J. Kim, S. Adachi and H. Ihee, *Phys. Rev. Lett.*, 2013, **110**, 165505.
53 Q. Kong, J. H. Lee, A. Plech, M. Wulff, H. Ihee and M. H. J. Koch, *Angew. Chem., Int. Ed.*, 2008, **47**, 5550–5553.
54 K. M. Knötig, D. Gust, T. Lenzer and K. Oum, *Photochem*, 2024, **4**, 163–178.
55 X. Niu, Z. Kuang, M. Planells, Y. Guo, N. Robertson and A. Xia, *Phys. Chem. Chem. Phys.*, 2020, **22**, 15743–15750.
56 T. Kim, J. Kim, H. Mori, S. Park, M. Lim, A. Osuka and D. Kim, *Phys. Chem. Chem. Phys.*, 2017, **19**, 13970–13977.
57 L. S. Bartell, E. A. Roth, C. D. Hollowell, K. Kuchitsu and J. E. Young, *J. Chem. Phys.*, 1965, **42**, 2683–2686.
58 D. F. Calef and P. G. Wolynes, *J. Phys. Chem.*, 1983, **87**, 3387–3400.
59 D. F. Calef and P. G. Wolynes, *J. Chem. Phys.*, 1983, **78**, 470–482.
60 H. Sumi and R. A. Marcus, *J. Chem. Phys.*, 1986, **84**, 4894–4914.
61 E. M. Kosower and D. Huppert, *Annu. Rev. Phys. Chem.*, 1986, **37**, 127–156.
62 A. Warshel and J.-K. Hwang, *J. Chem. Phys.*, 1986, **84**, 4938–4957.
63 P. F. Barbara, G. C. Walker and T. P. Smith, *Science*, 1992, **256**, 975–981.
64 M. A. Kahlow, T. J. Kang and P. F. Barbara, *J. Phys. Chem.*, 1987, **91**, 6452–6455.
65 Y. Sasaki and H. Hamaguchi, *Spectrochim. Acta, Part A*, 1994, **50**, 1475–1485.
66 Y. Yoneda, T. Konishi, K. Suga, S. Saito and H. Kuramochi, *J. Am. Chem. Soc.*, 2025, **147**, 12051–12060.
67 T. Yanai, D. P. Tew and N. C. Handy, *Chem. Phys. Lett.*, 2004, **393**, 51–57.
68 W. J. Hehre, R. Ditchfield and J. A. Pople, *J. Chem. Phys.*, 1972, **56**, 2257–2261.
69 P. C. Harihara and J. A. Pople, *Theor. Chim. Acta*, 1973, **28**, 213–222.
70 V. Barone and M. Cossi, *J. Phys. Chem. A*, 1998, **102**, 1995–2001.
71 S. Hirata and M. Head-Gordon, *Chem. Phys. Lett.*, 1999, **314**, 291–299.
72 F. Neese, *Wiley Interdiscip. Rev.: Comput. Mol. Sci.*, 2022, **12**, e1606.
73 F. Neese, *Wiley Interdiscip. Rev.: Comput. Mol. Sci.*, 2012, **2**, 73–78.
74 F. Plasser and H. Lischka, *J. Chem. Theory Comput.*, 2012, **8**, 2777–2789.
75 F. Plasser, *J. Chem. Phys.*, 2020, **152**, 084108.
76 G. Granucci, M. Persico and A. Zoccante, *J. Chem. Phys.*, 2010, **133**, 134111.
77 F. Plasser, M. Ruckenbauer, S. Mai, M. Oppel, P. Marquetand and L. González, *J. Chem. Theory Comput.*, 2016, **12**, 1207–1219.
78 F. Plasser, M. Barbatti, A. J. A. Aquino and H. Lischka, *J. Phys. Chem. A*, 2009, **113**, 8490–8499.
79 S. Mai, P. Marquetand and L. González, *Wiley Interdiscip. Rev.: Comput. Mol. Sci.*, 2018, **8**, e1370.
80 S. Mai, D. Avagliano, M. Heindl, P. Marquetand, M. F. S. J. Menger, M. Oppel, F. Plasser, S. Polonius, M. Ruckenbauer, S. Yinan, D. G. Truhlar, Z. Linyao, P. Zobel and L. González, *SHARC3.0: Surface Hopping Including Arbitrary Couplings – Program Package for Non-Adiabatic Dynamics*, 2023.
81 F. J. A. Ferrer and F. Santoro, *Phys. Chem. Chem. Phys.*, 2012, **14**, 13549.
82 J. Cerezo and F. Santoro, *J. Comput. Chem.*, 2023, **44**, 626–643.

